



ELSEVIER

Contents lists available at ScienceDirect

# Engineering Fracture Mechanics

journal homepage: [www.elsevier.com/locate/engfracmech](http://www.elsevier.com/locate/engfracmech)

## Experimental study on Fe-SMA-to-steel adhesively bonded interfaces using DIC

Wandong Wang<sup>a,\*</sup>, Ardalan Hosseini<sup>b,c</sup>, Elyas Ghafoori<sup>a,d</sup><sup>a</sup> Structural Engineering Research Laboratory, Swiss Federal Laboratories for Materials Science and Technology (Empa), 8600 Dübendorf, Switzerland<sup>b</sup> Simpson Strong-Tie, Pleasanton, CA 94588, USA<sup>c</sup> Department of Civil and Environmental Engineering, University of California, Davis, CA 95616, USA<sup>d</sup> Institute of Structural Engineering, Department of Civil, Environmental and Geomatic Engineering, ETH-Zürich, 8093 Zürich, Switzerland

### ARTICLE INFO

#### Keywords:

Debonding  
Fe-SMA bonded joints  
Nonlinearity  
DIC  
Cohesive damage

### ABSTRACT

This study aimed to reveal the interface behavior of iron-based shape memory alloy (Fe-SMA) strips bonded to metallic substrates in order to ensure the integrity of such joints. A series of single lap-shear tests was performed on Fe-SMA-to-steel adhesively bonded joints. The test results reveal that the bond strength can reach over 70% of the tensile strength of the Fe-SMA and the cohesive failure mode can be realized. It is identified that three energy dissipation mechanisms occurred during the debonding process, indicating that the experimentally obtained bond-slip relations represent more than the energy dissipation by the failure of the adhesive.

### 1. Introduction

The interface failure of adhesively bonded iron-based shape memory alloy strips (Fe-SMA) joints is crucial to be examined in order to ensure the structural integrity. This paper presents an experimental study on the interface failure behavior of Fe-SMA-to-steel adhesively bonded joints. This study was motivated by the development of a prestressed bonded Fe-SMA retrofitting system for the fatigue strengthening of metallic structures. A good understanding of the interface failure of the adhesively bonded Fe-SMA joints is essential to the development of the prestressed fatigue strengthening system using the Fe-SMA.

The prestressing technique has been explored to generate beneficial compressive stresses in fatigue cracked metallic parent structures to remedy the fatigue crack growth or completely arrest the crack growth [1–3]. Conventionally, carbon fiber reinforced polymer (CFRP) strips are prestrained and subsequently anchored mechanically to the parent structures for prestressed fatigue strengthening [3]. A more advanced fatigue strengthening method explores the prestressing effect of NiTi SMA wires embedded in CFRP patches [1,2]. The former method requires large space and heavy hydraulic jacks to prestress CFRP strips, while the later method requires costly NiTi SMA material and the fabrication of the patches is time and labor consuming.

To reap the benefits of using a prestressed reinforcement, while minimizing the cost and efforts associated with complicated prestressing procedures, an Fe-SMA was introduced in 2009 at the Swiss Federal Laboratories for Materials Science and Technology (Empa) [4]. Among various superior properties, Fe-SMAs exhibit a unique characteristic, often referred to as the shape memory effect (SME), which is the ability of the permanently deformed material at room temperature to recover its original shape partially after being heated to an elevated temperature, known as the activation temperature [5]. This interesting characteristic of Fe-SMAs can be

\* Corresponding author.

E-mail addresses: [wandong.wang@empa.ch](mailto:wandong.wang@empa.ch) (W. Wang), [ahosseini@strongtie.com](mailto:ahosseini@strongtie.com) (A. Hosseini), [elyas.ghafoori@empa.ch](mailto:elyas.ghafoori@empa.ch) (E. Ghafoori).

<https://doi.org/10.1016/j.engfracmech.2021.107553>

Received 11 July 2020; Received in revised form 22 November 2020; Accepted 13 January 2021

Available online 20 January 2021

0013-7944/© 2021 The Author(s). Published by Elsevier Ltd. This is an open access article under the CC BY license

(<http://creativecommons.org/licenses/by/4.0/>).

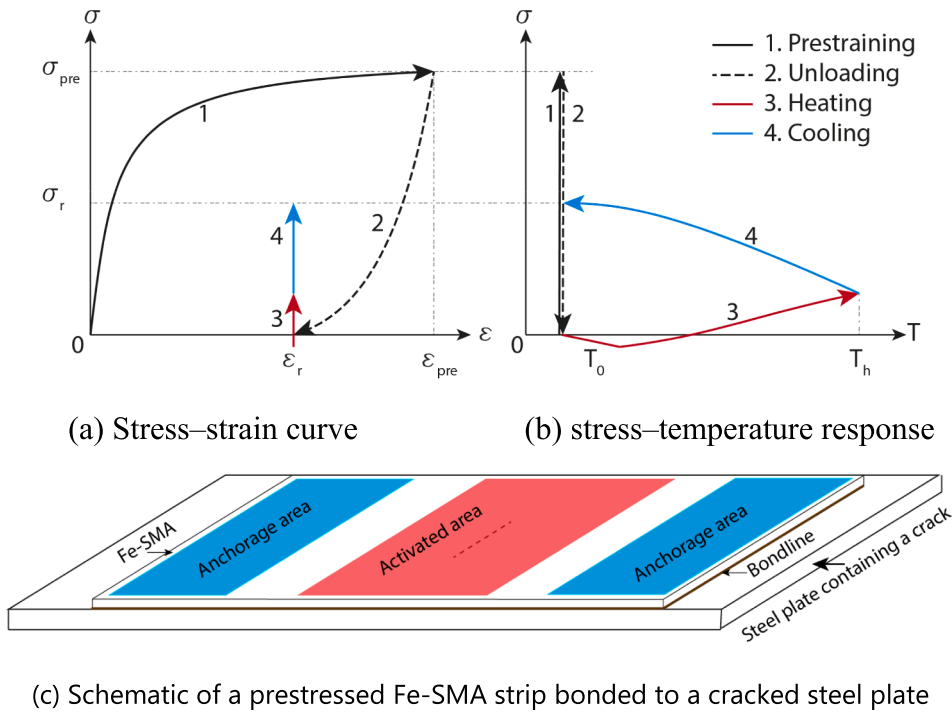


Fig. 1. Fe-SMA activation and prestressing.

exploited for the prestressed strengthening of existing metallic structures by securely fixing a deformed Fe-SMA reinforcement against the member of interest, and subsequently activating it through heating [6].

Owing to the advantages of Fe-SMA reinforcements for prestressed applications, several studies have been performed to characterize this novel material further [7–9]. Moreover, several experimental investigations have demonstrated the potential of Fe-SMAs for prestressed strengthening of steel structures [10–14]. A recent cost analysis revealed that even though the current price of Fe-SMA material is higher than that of normal modulus (NM) CFRPs, the end costs of both strengthening solutions are comparable [6]. This is mainly attributed to the relatively high cost of the mechanical clamping systems that are required for prestressed CFRP applications [6]. To date, end-anchorage in the form of friction-based mechanical clamps [13] or nail-based systems [14] have been developed for the Fe-SMA strengthening of metallic members. As mentioned earlier, the former anchorage system requires a more complicated design and manufacturing process that leads to an increased cost, whereas the latter is relatively inexpensive and easy to execute. However, nail-based anchorages [14] may not be the best solution for the strengthening of metallic structures that are subjected to cyclic loading (e.g., bridges), owing to concerns regarding their fatigue performance. On the contrary, adhesive bonding offers an even stress transfer between the reinforcement and parent structure and eliminates fatigue-prone structural interventions such as fastener holes; hence, adhesive bonding is a more desirable joining method in terms of fatigue performance [15]. Consequently, it is of great interest to investigate the feasibility of using adhesively bonded Fe-SMA strips for the strengthening of metallic structures.

To achieve this goal, the behavior of Fe-SMA strips bonded to a metallic substrate must be fully understood; this is the main objective of the current study, which, to the best of the authors' knowledge, has never been achieved so far. The interface in the adhesively bonded Fe-SMA joints represents the weakest point, the debonding failure can nullify the prestressed strengthening effects and lead to rapid crack growth in the parent structure and catastrophic failure. It is essential to be studied to ensure its structural integrity. Single lap-shear tests have been typically employed to study the interface behavior of reinforcements, normally CFRP strips, externally bonded to steel structures and mode II bond-slip relations have been obtained based on the experimental measurements for the fracture analysis of the debonding process [16]. Even though the debonding process of CFRP-to-steel joints has been fairly understood and the associated fracture analysis has been well established, the knowledge gained cannot be directly applied for the fracture analysis of the adhesively bonded Fe-SMA joints. The highly nonlinear constitutive behavior of the Fe-SMA, compared to linear elastic constitutive behavior of CFRP strips, results in added complications in understanding the debonding process and establishing corresponding fracture analysis methods. This paper presents a comprehensive experimental study to investigate the bond behavior of adhesively bonded interfaces between Fe-SMA strips and steel substrates. A single lap-shear test configuration, typically used to study CFRP-to-steel bonded interfaces, was adopted in the test campaign. An advanced three-dimensional (3D) digital image correlation (DIC) system was employed in all the tests to further investigate the full-field behavior of the bonded joints and obtain the bond-slip relations for various structural adhesives. Particular emphasis is placed on the effect of nonlinear behavior of the Fe-SMA on the debonding process and the obtained bond-slip relations. This test campaign was carried out as a first step towards the development of a prestressed bonded Fe-SMA solution for vast metallic structures.

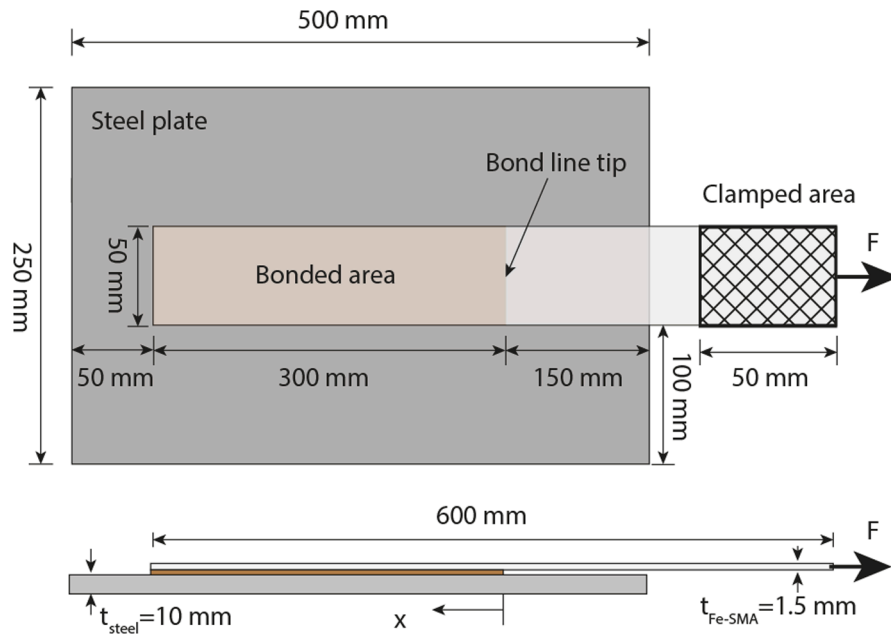


Fig. 2. Specimen configuration.

## 2. Fe-SMA activation and prestressing principle

As mentioned earlier, Fe-SMA materials exhibit an SME that allows for their easy activation and prestressing. Therefore, unlike with CFRP reinforcements, no mechanical loading is required to prestress an Fe-SMA reinforcement. To facilitate the understanding, a brief description of the activation and prestressing principle of the Fe-SMA is provided in this section. A schematic stress–strain and stress–temperature response of an Fe-SMA reinforcement is shown in Fig. 1. As can be seen from Fig. 1 (path 1), the Fe-SMA material is loaded at room temperature to  $\epsilon_{pre}$  (often 2%), which triggers a material phase transformation from austenite to martensite, also known as the forward phase transformation. Immediately thereafter, the Fe-SMA is fully unloaded as illustrated in path 2, leaving a residual strain of  $\epsilon_r$  in the material. The aforementioned loading and unloading cycle, referred to as prestraining, can be performed as the end phase of material production; therefore, no prestraining is required on site. In the next step, the Fe-SMA is heated to a target temperature of  $T_h$  while it is restrained at both ends. As clearly shown in Fig. 1b (path 3), the heating process first produces a compression in the restrained Fe-SMA as thermal expansion dominates initially. Nevertheless, a reverse phase transformation from martensite to austenite surpasses the thermal expansion as the temperature increases to the target temperature of  $T_h$ , and the material tends to recover its original condition. Upon cooling the Fe-SMA reinforcement to the ambient temperature (see path 4 in Fig. 1), tensile stresses are further generated in the Fe-SMA because of the thermal contraction of the restrained reinforcement. Finally, a recovery stress (prestress) of  $\sigma_r$  is generated in the Fe-SMA once it cools to the ambient temperature. It is worth emphasizing that the recovery stress  $\sigma_r$  is up to 360 MPa for a typical  $T_h$  of 160 °C [4,13,17]. As providing a detailed explanation on the SME and activation process of Fe-SMAs is beyond the scope of the current study, readers are directed to two previous studies [9,18] for further discussions on this topic.

A schematic of the envisaged fatigue strengthening method using the Fe-SMA is shown in Fig. 1(c). It is critical to avoid the complications, such as prestressing loss, deteriorated load transfer capability, associated with the softening of the adhesive over the anchorage areas during the activation process, see Fig. 1(c). Fortunately, heating the middle part of the Fe-SMA only to generate prestressing without softening the adhesive over the anchorage areas is achievable. A viable technique is to use two electrodes and run current to rapidly activate the Fe-SMA in-between. This technique has been used to activate NiTiNb SMA fibers embedded in CFRP, softening of the resin matrix 20 mm away from the electrodes during the activation was successfully avoided [2,19]. As a result, the effect of high temperature on the debonding behavior of Fe-SMA-to-steel joints is not investigated in this study.

## 3. Experimental program

A series of single lap-shear tests on adhesively bonded iron-based SMA-to-steel joints was performed at the Structural Engineering Research Laboratory of Empa. Detailed descriptions of the specimen details and preparation, material properties, test set-up, instrumentation and loading procedure used in this test campaign are presented in this section.

### 3.1. Specimen details and preparation

The specimen configuration is illustrated in Fig. 2. An Fe-SMA strip of thickness 1.5 mm and width 50 mm is adhesively bonded to a

**Table 1**  
Specimen details.

Specimen ID	Adhesive	$t_a$ [mm]	Bond length [mm]	Curing method
Sika-1	Sika 1277	0.35	300	RT <sup>a</sup>
Sika-2	Sika 1277	0.45	300	RT
3M-1	3M EC9323	0.2	300	RT
3M-2	3M EC9323	0.18	300	RT
EA-RT	Hysol EA9394	0.12	300	RT
EA-HR	Hysol EA9394	0.13	300	HR <sup>b</sup>

<sup>a</sup> RT: room temperature curing.

<sup>b</sup> HR: elevated temperature curing at 82 °C for two hours.

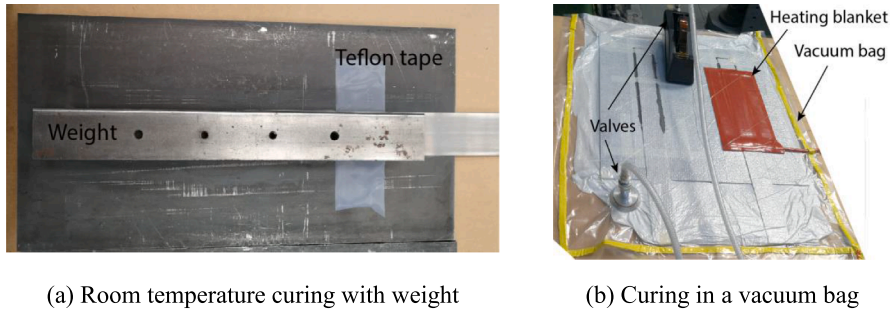


**Fig. 3.** Specimen manufacturing.

steel plate over a bond length of 300 mm. The dimensions of the Fe-SMA strip and the steel plate are provided in Fig. 2. The other end of the Fe-SMA strip is clamped in a mechanical grip to apply the lap-shear load. The Fe-SMA strips were not prestressed, because the main purpose of this study was to investigate the Fe-SMA-to-steel bond behavior, and not the prestressing effects of the Fe-SMA material. In total, six specimens were manufactured using three different two-component adhesives. An overview of the test matrix is provided in Table 1. The thicknesses of the adhesives,  $t_a$ , for all specimens are also listed in this table.

A similar lap-shear specimen configuration with steel plate substrates (instead of steel I-beams) has been adopted by other researchers to study the mode-II fracture behavior of CFRP-to-steel bonded interfaces [20,21]. The specimen configuration adopted in this study facilitates the preparation and handling of the specimens for such tests. The steel plate is sufficiently rigid to eliminate the out-of-plane deformation when it is fixed to the test setup to study the mode-II fracture behavior of the Fe-SMA-to-steel interfaces. The test setup is explained in the next subsection.

The surfaces of both the steel plates and Fe-SMA strips were carefully prepared before bonding. They were thoroughly cleaned with white wipes soaked with acetone prior to sand-blasting. This was performed to prevent the contaminants on the surface from spreading to the fresh surface formed after sand-blasting [22]. The surfaces were grit-blasted using 0.15–0.21 mm aluminum oxide at a pressure of 8 bar. The grit-blasted surfaces were thoroughly cleaned with acetone again before applying the adhesive to bond the two substrates together. The respective adhesive was prepared as per its technical data sheet. The bonding was performed within 2 h after grit blasting the substrate surfaces. A strip of Teflon tape of thickness 0.056 mm was placed between the Fe-SMA strip and the steel plate in order to control the bond length, as shown in Fig. 3(a).

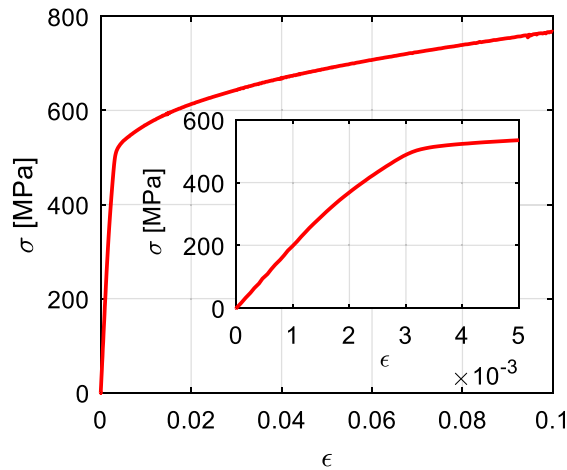
Two techniques were used to hold the two adherends together during the curing process. For specimens with the Sika1277 and 3M EC9323 adhesives that are listed in Table 1, a pressure of approximately 0.003 MPa was applied to the Fe-SMA strip surface after the application of the adhesive throughout the curing process in a climate room at Empa laboratory. Fig. 3(a) shows a steel bar placed on the Fe-SMA strip to apply pressure during the curing process. The specimens were tested after 14 days in the climate room at a controlled temperature of  $23 \pm 0.5$  °C. For specimens with the Hysol EA9394 adhesive, as shown in Fig. 3(b), a vacuum bag was employed to apply a uniform pressure of 0.086 MPa on the Fe-SMA strips. This technique was applied to overcome the problem associated with the relatively high viscosity of Hysol EA9394 when the first technique was used [23].

Fig. 3(b) shows the EA-RT and EA-HR specimens inside the vacuum bag, which was connected to two valves. A heating blanket was also placed on top of the Fe-SMA strip over the bonded area of the EA-HR specimen inside the vacuum bag, as shown in Fig. 3(b). A hot bonder (BriskHeat® ACR®3 Hot Bonder, USA) was used to control the heat and vacuum during the curing process. One of the valves was connected to the built-in electric vacuum pump and the other to the vacuum gauge of the hot bonder. A vacuum pressure of 0.86 bar, equivalent to 0.086 MPa, was established and maintained for 24 h for both specimens. The temperature profile of the heating process consisted of a ramp-up process at a rate of 2 °C/min, a dwell process at 82 °C for 2 h, and a natural (air) cooling process to cool the specimens to room temperature. Several thermocouple sensors were placed between the heating blanket and the specimen surface to monitor and control the temperature.

**Table 2**  
Material properties of adhesives and Fe-SMA.

Property	Sika1277 [24]	3M EC9323 [25,26]	Hysol EA9394 [23]	Fe-SMA [9,13,17]
Young's modulus [GPa]	2	2.65	4.24	~160
Tensile strength [MPa]	30	34	46	~1000
Viscosity [Pa·s]	A <sup>a</sup> : 430; B <sup>b</sup> : 100	A: 18; B: 700	A: 400–800; B: 20–70	NA
Elongation at break [%]	4	1.62	1.66	~ 40–50
Tensile lap-shear strength [MPa]	28	28	28.9	NA

<sup>a</sup> A refers to Part A of the two-component adhesive;  
<sup>b</sup> B refers to Part B of the adhesive



**Fig. 4.** Stress–strain curve of the Fe-SMA material. The inset shows that the Young's modulus of the Fe-SMA varies for strains less than 0.2%.

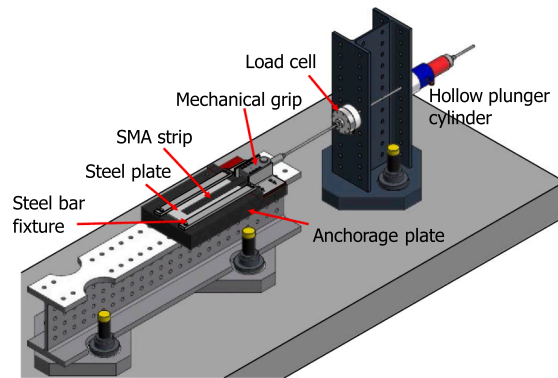


**Fig. 5.** Lap-shear test setup.

3.2. Material properties

The mechanical properties of the steel substrate, adhesives, and Fe-SMA used to manufacture the specimens are summarized in this section. The grade of the steel substrate is S355J2 + M, with a nominal yield strength and elastic modulus of 355 MPa and 210 GPa, respectively. The Fe-SMA-to-steel specimens were manufactured using three different adhesives. For comparison, the properties of the three adhesives are summarized in Table 2. As can be observed from Table 2, the Sika1277 adhesive is highly ductile with a 4% elongation at break.

The tensile mechanical behavior of the Fe-SMA is of particular interest; the mechanical properties are summarized in Table 2, according to test data from different studies [9,13,17]. Depending on the batches of the Fe-SMA material, small variations in the measured mechanical properties are expected. A slender Fe-SMA strip with dimensions of 300 × 15 × 1.5 mm<sup>3</sup> from the same batch used in the Fe-SMA-to-steel joints was therefore tested under quasi-static tensile loading to obtain a stress–strain curve, as shown in Fig. 4. The test was conducted using a static/fatigue testing machine with a 100 kN load cell. A clip-on extensometer with a gauge

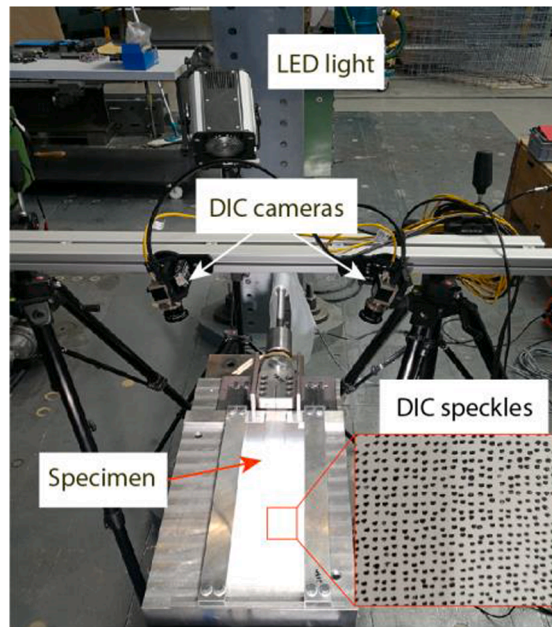


Fig. 6. DIC setup.

length of 15 mm ( $\pm 2$  mm measuring range) was used to monitor the strain. The tensile specimen was loaded under strain-controlled conditions, with a strain rate of 0.15%/s and a data acquisition rate of 0.05 s.

As can be observed from Fig. 4, the tensile behavior of the Fe-SMA is highly nonlinear and ductile compared to that of unidirectional CFRP plates commonly used for steel strengthening applications [6]. The Young's modulus of the Fe-SMA is not constant and starts to change for strain values below 0.2%, owing to the forward austenite-to-martensite phase transformation when the material is loaded [18]. The change in modulus is clearly shown by the nonlinear stress–strain curve in the inset of Fig. 4. When the strain value reaches 0.3%, the plastic deformation occurs and the material exhibits a highly ductile behavior. As a result of the nonlinear tensile behavior of the Fe-SMA, the well-established analysis methods (e.g., [27]) for lap-shear tests on CFRP-to-steel joints are not applicable for the Fe-SMA bonded joints. It is noteworthy that the stress–strain behavior of the Fe-SMA is shown for the strain only up to 10%, owing to the limit of the measuring range of the extensometer, not owing to the strength of the material. As shown in Table 2, the elongation at break of the Fe-SMA can reach as high as 40–50%.

### 3.3. Test setup

The single lap-shear test setup was employed to examine the interface bond behavior of Fe-SMA-to-steel joints in this study. Fig. 5 shows the test setup that was designed to perform the test. The steel plate of the specimen was fixed to the anchorage plate containing a horizontal constraint with two steel bar fixtures to eliminate any rigid-body movement of the specimen during testing. The lap-shear load was applied to the Fe-SMA strip through a mechanical grip that clamped the strip end (see Fig. 2). An MTS load cell with a capacity of 300 kN, connected between the mechanical grip and the cylinder by high-strength M13 threaded steel rods, was used to monitor the applied load. The setup was aligned to eliminate any eccentricities in the load path.

### 3.4. Instrumentation and loading procedure

A noncontact and full-field 3D DIC technique was used to monitor the displacement and strain fields during the test. Fig. 6 depicts the setup of the DIC system. A VIC-3D 8 system (Correlation Solutions, Inc.) with two 12 MP (4000  $\times$  3000) cameras was used. The DIC method acquires the displacement field of the specimen surface by tracking the displacements of random speckles in a reference image of the unloaded specimen without any deformation and in an image of the deformed specimen [28]. The displacement field can be then post-processed to obtain the strain field.

To facilitate the correlation, white paint was applied on the specimen surface and a random black speckle pattern was applied on the white background, as shown in the magnified image in the inset of Fig. 6. A pattern application kit provided by Correlation Solutions, Inc. was used to apply consistent black speckle patterns on all the specimens. The size of the applied black speckles was 3.3 mm. The DIC system was carefully calibrated prior to executing each test.

The load cell was synchronized with the DIC system, and the frame capture speed was set to 1 Hz during testing. The analyzed displacement and strain results for each DIC image correspond to a certain load level. The load was applied with a (manual) hydraulic jack until the joint failed.

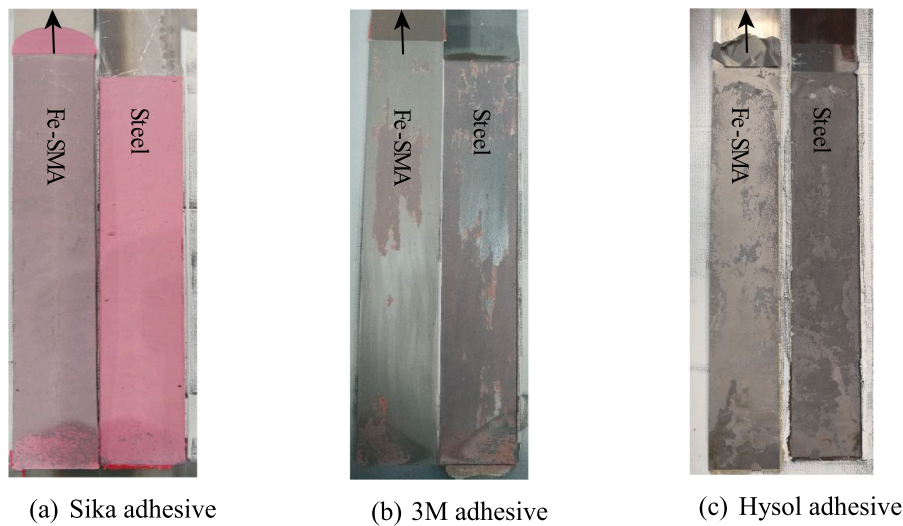


Fig. 7. Fracture surfaces.

**Table 3**  
Bond strengths.

Specimen ID	adhesive	Failure mode	Load capacity [kN]	Axial stress [MPa]	Effective bond length [mm]	Average load capacity [kN]
Sika-1	Sika 1277	Cohesive	56.78	757.07	115	57.15
Sika-2	Sika 1277	Cohesive	57.52	766.93		
3M-1	3M EC9323	Adhesive	54.61	728.13	90	53.79
3M-2	3M EC9323	Adhesive	52.96	706.13		
EA-RT	Hysol EA9394	Cohesive/ adhesive	52.19	695.87	90	–
EA-HR	Hysol EA9394	Cohesive/ adhesive	49.71	662.8	70	–

#### 4. Test results

This section summarizes the directly obtained experimental results for different specimens with different adhesives. They include the fracture failure mode in the bond line, measured bond strengths, load–slip behavior and axial strain distribution on the Fe-SMA strip surface.

##### 4.1. Fracture surface examination

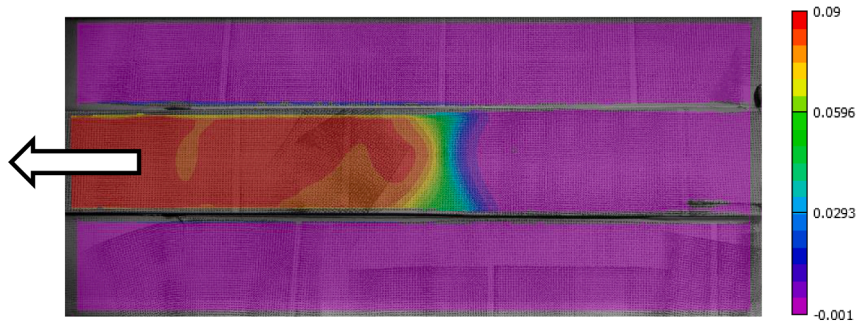
The fracture surfaces were examined to understand their failure modes upon completion of the lap-shear tests. The typical fracture surfaces of specimens with the three tested adhesives are presented in Fig. 7.

Fig. 7(a) shows the fracture surfaces of the specimen with the Sika1277 adhesive that failed in the cohesive failure mode. A layer of adhesive can be observed on the surfaces of both the Fe-SMA and steel substrates, with a very thin layer of adhesive covering the Fe-SMA. An adhesive failure at the interface between the adhesive and the Fe-SMA can be observed for the specimen with the 3M EC9323 adhesive, as shown in Fig. 7(b). A small portion of the failure is at the steel/adhesive interface. As can be seen from Fig. 7(c), for the specimen with the Hysol EA9394 adhesive, the failure mode is a combination of the cohesive and adhesive failure modes. However, the adhesive failure at the interface between the Fe-SMA and the adhesive is the dominant failure mode.

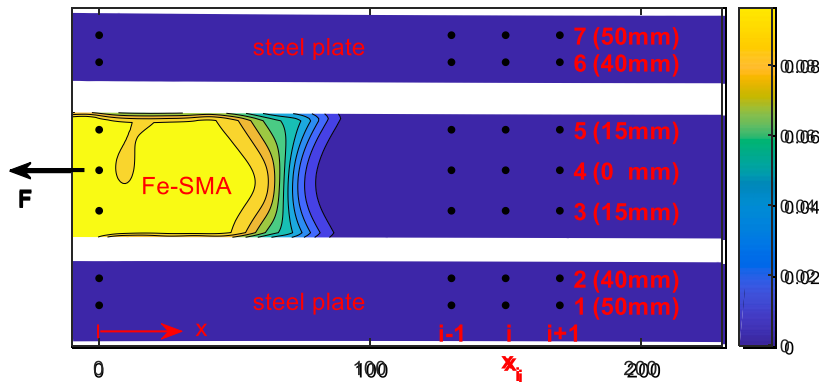
Another feature is that the length of the portion of the Fe-SMA strip that was bonded to the steel plate (i.e., initial 300 mm bond length) increased after the test. Prominent elongations in the loading direction can be observed in the Fe-SMA strips in Fig. 7. The permanent deformation of the Fe-SMA strips demonstrates that the strips were plastically deformed.

##### 4.2. Bond strengths

The bond strengths of all the tested specimens are summarized in Table 3. The load capacity was directly measured using the load cell in this study. The tested specimens can be categorized into three groups corresponding to the three adhesives used to manufacture them. Based on the data summarized in Table 3, it can be seen that each pair of specimens with the same adhesive have very close and consistent load capacities. The specimens with the Sika1277 adhesive have the greatest load capacity of approximately 57 kN. As discussed above, these two specimens exhibited the cohesive failure mode. Even though the specimens with the 3M EC9323 adhesive



(a) Typical strain field obtained using the DIC technique. The result shown is for Sika-1 at  $F = 56.5$  kN.



(b) Data processing using DIC measurements. The result shown is for Sika-2 at  $F = 56.4$  kN

Fig. 8. Post processing of DIC measurements.

failed in the adhesive failure mode, their bond strengths are very close to those of specimens Sika-1 and Sika-2. The specimens with the EA9394 adhesive have the lowest load capacity; nevertheless, the bond strengths for these two specimens are approximately 50 kN. Furthermore, it can be observed from Table 3 that (based on the single result obtained in this study) the hot curing condition does not improve the bond strength for the Hysol EA9394 adhesive.

The corresponding axial stresses in the Fe-SMA at the ultimate load capacities of the joints are also provided in Table 3. As can be seen, the ultimate stress levels in the Fe-SMA strips at debonding are roughly twice the recovery stress  $\sigma_r$  that can be achieved with the typical  $T_h$  of 160 °C.

The effective bond lengths for the different joints are also summarized in Table 3. A detailed description of the effective bond length is presented in Section 5.

#### 4.3. DIC results and post-processing techniques

The measurements obtained using the DIC technique are used to acquire the essential information to study the bond behavior of the Fe-SMA-to-steel bonded joints. Fig. 8 depicts typical strain distributions obtained with the DIC technique and the scheme of extracting DIC measurements for further calculations. The procedure for determining the bond-slip relations of FRP-to-steel bonded joints is adopted for the tested configurations [16]. Essentially, the strain distribution on the externally bonded strip is used to solve for the shear stress distribution in the bond line and the slip distribution. The post-processing procedure is detailed in this section.

The acquired DIC images were post-processed by using the VIC-3D software to obtain the displacement and strain fields on both the steel plate and Fe-SMA strip surfaces. An image of typical strain fields after post-processing is shown in Fig. 8(a). As can be seen, the values of the strain distributions on the steel plate surface and on the bonded Fe-SMA strip are very small. The debonded part of the Fe-SMA strip has a relatively high strain level. At the debonding crack tip, a steep strain gradient on the Fe-SMA strip surface can be observed. The shear stresses considerably restrain the strain deformation of the Fe-SMA strip. However, the bond line is heavily loaded at the crack tip under shear and debonding propagates when the critical fracture energy is exceeded.

To determine the interfacial shear or bond-slip behavior for the tested adhesives and interfacial shear stress distributions in the bond line, the displacement and strain fields obtained from the DIC technique must be further post-processed. As illustrated in Fig. 8

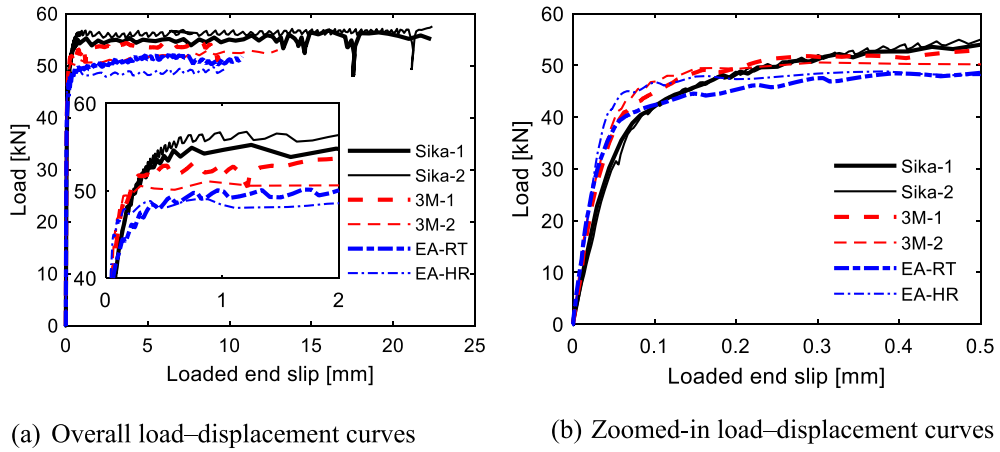


Fig. 9. Load-slip curves.

(b), the longitudinal displacement and strain values at the locations of discretized grid nodes are used. A longitudinal x-axis coordinate system is used to denote the distance from the loaded end. The loaded end is chosen as the origin of the longitudinal x-axis. Data from  $x = 0$  to  $x = 200$ mm are extracted using an increment interval of 2 mm between the two columns of data points, i.e., the distance between column  $i - 1$  and column  $i$  is 2 mm. Each column has seven points, as shown in Fig. 8(b). Three points are on the Fe-SMA strip and two points are on the steel on each side of the Fe-SMA strip. Their relative distances from the middle of the Fe-SMA strip are illustrated in Fig. 8(b).

The slip of the Fe-SMA strip is crucial for the interfacial stress behavior analysis. It can be calculated by subtracting the average displacement of the steel plate from that of the Fe-SMA strip, as expressed in Eq. (1).

$$\delta_i = \frac{U_{3,i} + U_{4,i} + U_{5,i}}{3} - \frac{U_{1,i} + U_{2,i} + U_{6,i} + U_{7,i}}{4} \tag{1}$$

where  $\delta_i$  is the slip of the Fe-SMA at  $x_i$ .  $U$  denotes the longitudinal displacement of each data point and the subscripts 1 to 7 refer to the seven points of the  $i$ th column.  $U$  is defined as positive when it is in the loading direction, as shown in Fig. 8(b).  $\delta_0$  denotes the slip at the loaded end.

Similarly, the strain in the Fe-SMA strip is calculated from the derivatives of the displacements in Eq. (1):

$$\epsilon_i = \frac{\epsilon_{3,i} + \epsilon_{4,i} + \epsilon_{5,i}}{3} - \frac{\epsilon_{1,i} + \epsilon_{2,i} + \epsilon_{6,i} + \epsilon_{7,i}}{4} \tag{2}$$

where  $\epsilon_i$  refers to the real strain at  $x_i$  of the Fe-SMA strip.  $\epsilon_{j,i}$  is the DIC-calculated strain value at point  $j$  ( $j = 1 \dots 7$ ) in column  $i$ . Eq. (2) is used to obtain the strains on the Fe-SMA strip more accurately. Unlike strain gauges that measure strains by directly measuring deformation, the DIC method calculates strains based on displacement field measurements. For the adopted test setup, the displacement field on the Fe-SMA strip includes the contribution of the displacement of the steel plate. As a result, the directly calculated strain values, i.e.,  $\epsilon_{3,i}$ ,  $\epsilon_{4,i}$ , and  $\epsilon_{5,i}$  on the Fe-SMA strip include negligible strain contributions of the steel plate. The real strain is therefore obtained with Eq. (2).

Once the real strain distribution of the Fe-SMA strip is determined, the stress distribution can be calculated. Unlike a CFRP strip, which deforms elastically in similar single lap-shear tests, the deformation of the Fe-SMA strip in this study exhibits a significant degree of plasticity. The method adopted here to calculate the stress in the Fe-SMA for given strains relies on numerical interpolation. The experimentally obtained stress-strain data points graphically shown in Fig. 4 are known, and the stress values for any strains calculated by Eq. (2) are estimated by interpolation; the cubic spline interpolation technique is adopted in this study.

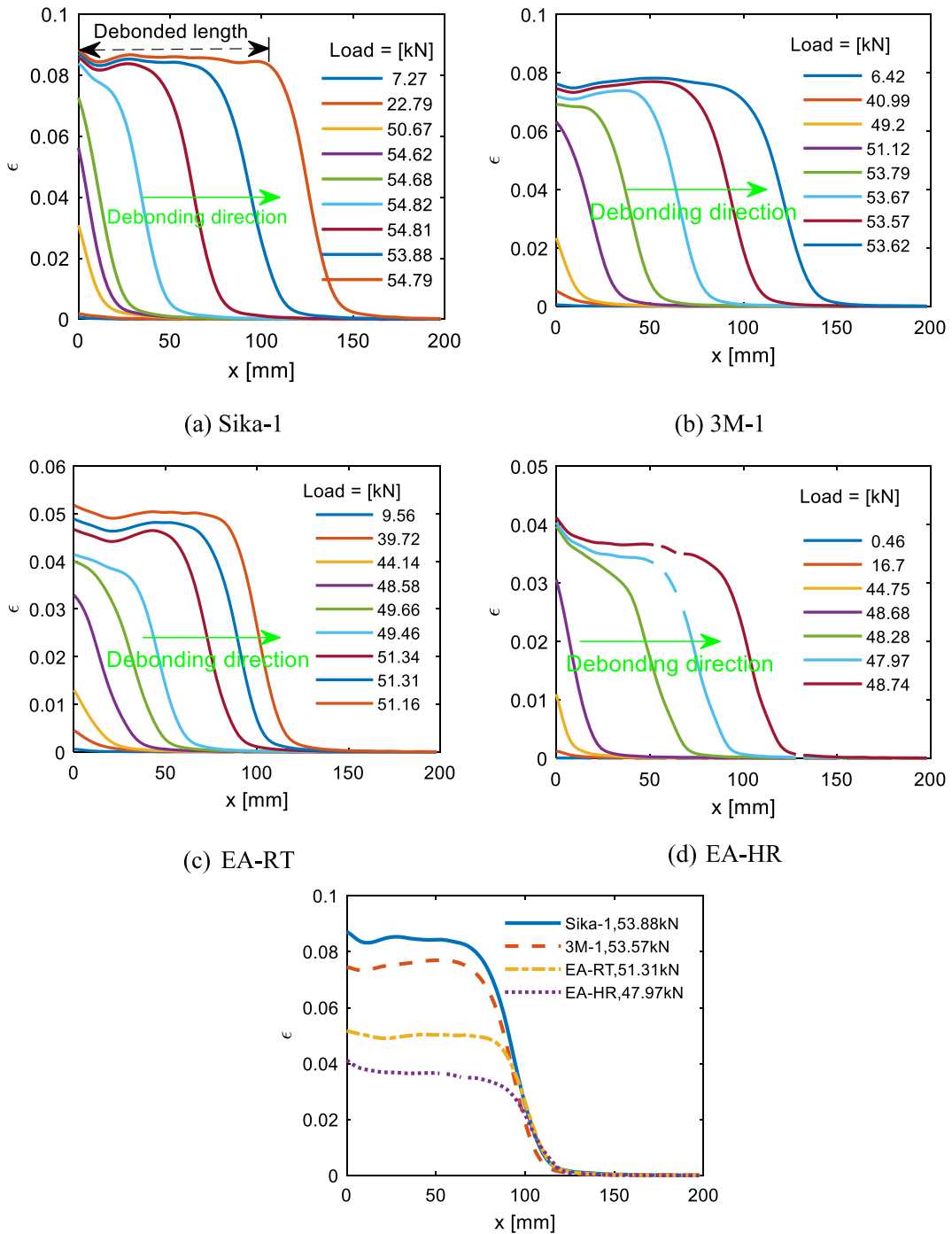
Based on the equilibrium, the shear stress,  $\tau_i$ , at  $x_i$  is calculated as

$$\tau_i = \frac{\sigma_{i-1} - \sigma_{i+1}}{x_{i+1} - x_{i-1}} t_{SMA} = \frac{\sigma_{i-1} - \sigma_{i+1}}{\Delta} t_{SMA} \tag{3}$$

where  $\sigma_{i-1}$  and  $\sigma_{i+1}$  are axial stresses in the Fe-SMA estimated by using the interpolation method at  $x_{i-1}$  and  $x_{i+1}$ , respectively;  $\Delta = x_{i+1} - x_{i-1}$  represents the interval space. It is worth noting that the stress relaxation in the Fe-SMA strip introduces an erroneous bias to the calculated shear stresses according to Eq. (3). The stress relaxation of the Fe-SMA is a stress level and time dependent process, meanwhile the loading rate could not be strictly controlled using the test setup, this bias therefore cannot be eliminated or quantitatively analyzed in this study. Qualitative analyses of the error in the calculated shear stresses are provided in subsequent sections.

Based on the analysis described in Appendix A,  $\Delta = 4$ mm is chosen for the analysis. This choice is based on the trade-off between a high resolution and a minimized error in the results.

In Appendix A, a discussion on how the interval is specified for the data post-processing is presented. Two factors are considered for



(e) Comparison of strain distributions at ultimate loads

Fig. 10. Evolution of axial strain distributions in tested specimens.

determining the interval: (1) the noise levels in the DIC measurements and calculated shear stresses, and the (2) spatial resolution, which should be sufficiently high to capture the high shear stress gradient in the fracture process zone (FPZ). More details regarding the effect of the measurement intervals on the shape of the bond-slip models as well as the peak shear stress can be found in Appendix A.

#### 4.4. Load–slip behavior

Fig. 9 summarizes the load–slip curves for all the tested specimens with different adhesives. The slip of the loaded end is calculated with Eq. (1) using the longitudinal displacements of data points in the first column at  $x = 0$ . The load values are taken directly from the load cell measurements.

As can be seen from Fig. 9(a), the load–slip curves for all the adhesives exhibit a long plateau before the final failure and the loaded-end slip for the Sika adhesive reaches 20 mm. The inset in Fig. 9(a) shows that the plateau starts after 0.5 mm slip for all the specimens. The long plateau is attributed to the fact that a large bond length of 300 mm that allows for a stable debonding process was adopted for all the test configurations. The extremely large slip of the loaded end is due to the large plastic deformation of the Fe-SMA strip. The Fe-SMA instantly plasticized once debonded from the steel plate, which contributed to the large slip of the loaded end.

The load–slip curves of the two specimens for each adhesive are quite consistent. Overall, the failure behavior of the Sika-1 and Sika-2 specimens is more ductile than those of the other two types of specimens, as can be observed from Fig. 9(a). The initial stiffness of the load–displacement curves can be observed better in Fig. 9(b). Even though the load capacity of the Sika1277 adhesive is higher, it has a lower initial stiffness (see Fig. 9(b)) compared than the other two adhesives do; this is attributed to its lower Young's modulus [29].

As a result of the large deformation of the Fe-SMA strip during testing, the stroke limit of the hydraulic actuator was reached, and the test had to be paused a few times. The movement of the rod connecting the grip head and the actuator, shown in Fig. 5, was fixed with reserved nuts, and the hydraulic actuator was adjusted to continue to apply tensile loads to the Fe-SMA strip to conclude the test. During this time, the load in the Fe-SMA strip decreased slightly, which was due to a stress relaxation phenomenon in the alloy [7]. Nevertheless, the load was restored after the test was resumed. The large fluctuations in Fig. 9(a) refer to these decreases and increases in stress.

Previous studies have shown that the stress relaxation in the Fe-SMA is due to a reversible phase transformation-induced deformation (i.e., forward austenite-to-martensite transformation) rather than an irreversible plasticity [9]. The stress relaxation is known to be one of the main parameters that contributes to the nonlinear behavior of the Fe-SMA material (see path 1 in Fig. 1(a)) [18]. The amount of reduced stress is greater during the first few minutes (i.e., 0–15 min) after loading and depends on the loading rate and the absolute stress level [7].

#### 4.5. Axial strain distribution along the Fe-SMA strip

The typical strain distributions on the Fe-SMA strips of the tested specimens are summarized in Fig. 10. The strain values are calculated with Eq. (2). The overall strain distributions of all specimens follow the same trend. For all specimens, significant strains only developed within a short bond length near the loaded end before their ultimate loads were reached. A debonding process can be recognized as a plateau in the evolution of the strain distributions of all specimens once the ultimate load is reached (see the indicated debonding region in Fig. 10(a) as an example). The small fluctuation in the strains near the loaded end during the debonding process is due to the nonlinearity of the material and stress concentration at the loaded end [16].

Compared to the development of strain distributions in conventional CFRP-to-steel bonded joints [16,29,30], the development of strains in the Fe-SMA strips observed in this study is quite different. In CFRP-to-steel specimens, the maximum strain in the CFRP strip is reached once the ultimate load is reached, and the maximum strain does not increase during the debonding process. On the contrary, the maximum strain level in the Fe-SMA strips increased after the ultimate load was reached, as can be observed in Fig. 10. This phenomenon is due to the nonlinear constitutive behavior of the Fe-SMA, as shown in Fig. 4. The Young's modulus of the Fe-SMA decreases substantially after the strain reaches 0.3–0.35%. A small increase in the stress would result in a large increase in the strain of the Fe-SMA strip thereafter. Even before the ultimate load is reached, a large region of the Fe-SMA near the loaded end has strain values larger than 0.35%. Another reason for this phenomenon is the relaxation mechanism of the Fe-SMA [7]. Upon loading, the stress in the Fe-SMA decreases to a certain degree when the strain remains the same. To sustain the ultimate load during testing, the strains kept increasing.

The strain distributions presented in Fig. 10 reflect the bond capacities of the four specimens. The Sika adhesive provides the highest load capacity for such bonded joints, as can be seen from Table 3. It is reasonable that the maximum strain in the Sika-1 specimen is the highest among those of all the specimens. It is worth noting that the 3M-1, EA-RT and EA-HR specimens experienced adhesive failure. The low bond capacities of these three specimens are mainly a result of this failure mode.

Careful scrutiny of Fig. 10(e) reveals that the distinction in the strain levels in the Fe-SMA strips are highly pronounced among the different specimens tested, even though the difference in the ultimate loads of the four specimens is relatively small. This pronounced difference in the strains can be attributed mainly to the large plastic deformation of the Fe-SMA for small increments in the stresses. The increased stress, due to a small increase in load, results in a pronounced increase in the strain level after the material has become highly ductile. As can be seen in Fig. 4, all the tested specimens reached this highly ductile region of the Fe-SMA.

As mentioned earlier, the accumulated effect of the stress relaxation mechanism in the Fe-SMA is also a contributing factor. According to the strain–stress relation of the Fe-SMA shown in Fig. 4, the ultimate load of EA-RT should result in a strain of 0.048, whereas the ultimate load of the Sika-1 should result in a strain of 0.075. However, the measured maximum strains for both specimens (Fig. 10) are 0.051 and 0.088 respectively that are higher than the expected values, owing to the stress relaxation mechanism. A longer time and greater stress are needed for the Sika-1 specimen to reach the ultimate load than those for the EA-RT specimen; this allows the strains due to the stress relaxation mechanism to accumulate more.

From the aforementioned results, it is observed that the bond behavior of the Fe-SMA-to-steel joints is considerably affected by the

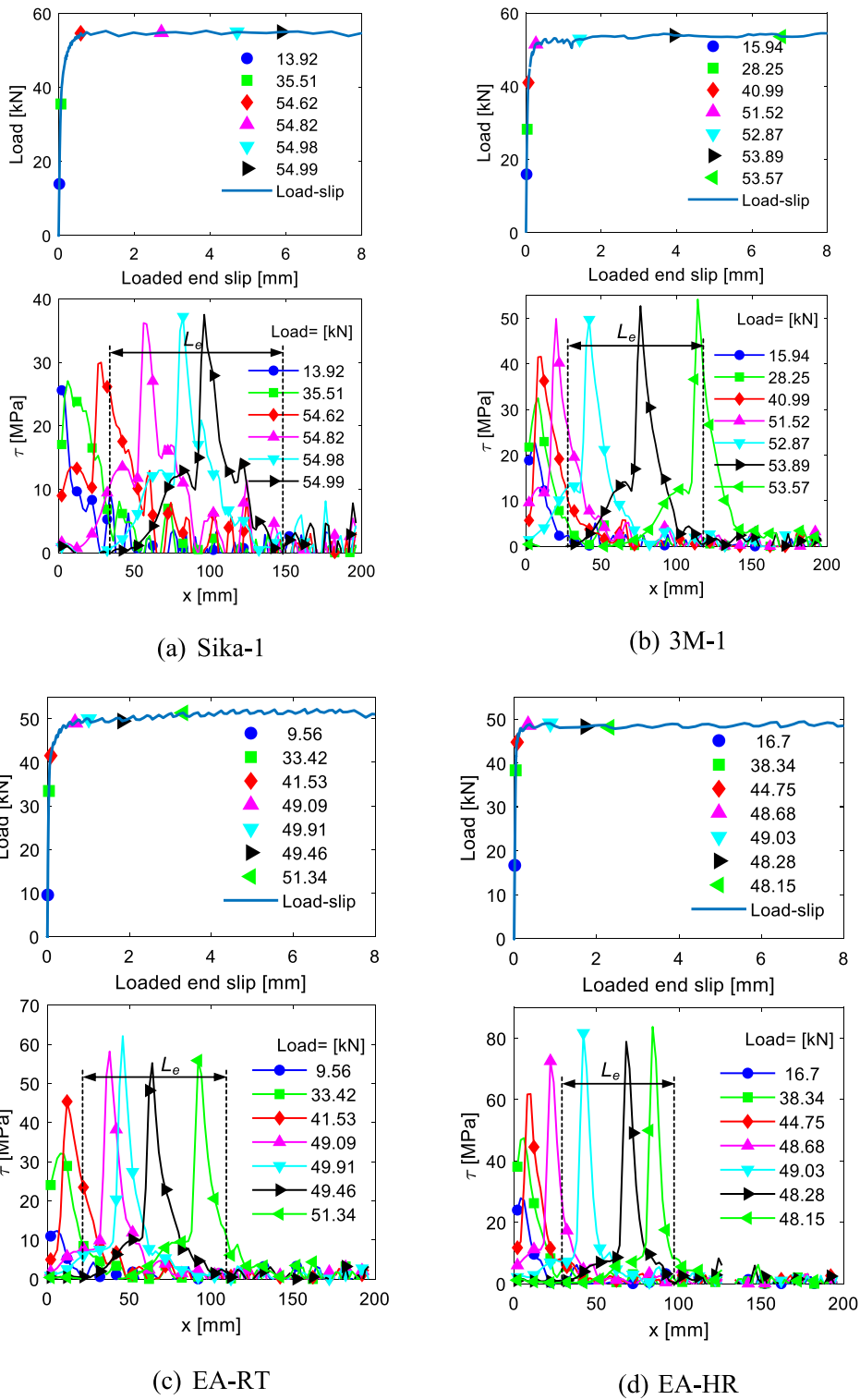


Fig. 11. Evolution of interfacial shear stress profiles.

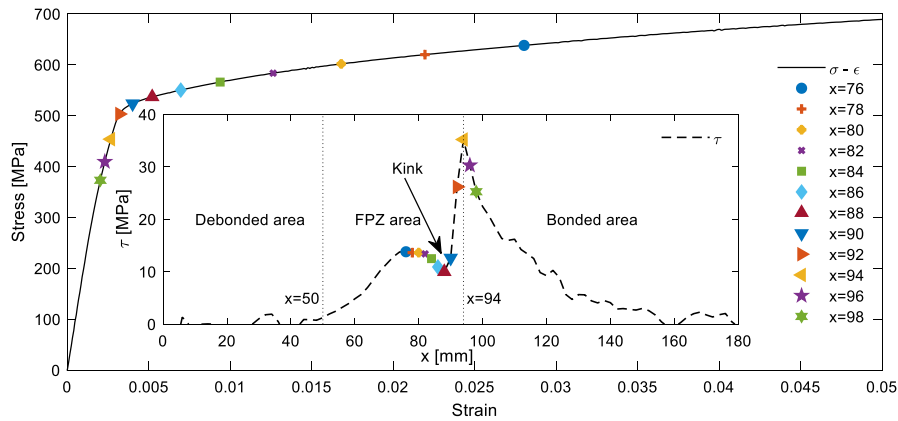


Fig. 12. Study of the kink in the shear stress distribution. Data were obtained from the Sika-2 specimen at  $F = 55.86$  kN.

loading rate, which is mainly due to the time-dependent stress relaxation in the Fe-SMA [18]. It should be noted that this is unlike the behavior typically observed in conventional CFRP-to-steel joints.

### 5. Interfacial shear stress distribution and effective bond length

The evolution of the interfacial shear stress distributions for different specimens at various phases of the debonding process are presented in Fig. 11. The interfacial shear stress distributions along the Fe-SMA strip is calculated using Eq. (3). The stress distributions for specimens Sika-2 and 3M-2 are very similar to those shown in Fig. 11 (a) and (b), respectively. Therefore, they are excluded herein for the sake of brevity. Overall, the interfacial shear stress distributions for all the specimens seem to follow the same pattern, which is expected because all the adhesives have comparable Young's moduli and similar ultimate tensile strengths (see Table 2).

As can be seen in Fig. 11, the development of the shear stress distributions for all the specimens follows a similar pattern. When the load is relatively small, as shown by lines with blue circles in the respective subfigures for all the specimens, the stress at  $x = 0$  mm has the highest value and decreases along the bonded length (i.e., the  $x$ -axis). The slip along the Fe-SMA is still in the ascending branch of the bond-slip relation of the adhesive, with the loaded end having the highest slip. Before the ultimate load capacity of the bond is reached, the shear stress at the loaded end,  $x = 0$  mm, has entered the descending branch of the bond-slip relation for the joint. This phenomenon is clearly shown by the lines with green squares in Fig. 11. The low peak shear stress at the loaded end could be attributed to the stress concentrations at the loaded end, which results in a mixed-mode failure mechanism at  $x = 0$  mm. The debonding process is initiated before the ultimate load capacity is reached. Unlike the CFRP-to-steel bonded joints, where the nonlinearity in the load-slip curve is purely attributed to the initiation of localized debonding at the loaded end, in this case, the nonlinearity is due to a combination of the localized debonding and the nonlinear constitutive behavior of the Fe-SMA.

Finally, the debonding process starts when the shear stress at the loaded end reaches zero. As can be seen, the shear stress curves shift to the free end of the bonded joint under approximately constant loads; a plateau is observed in the load-slip curve, and the shape of the shear stress curves remains nearly unchanged.

As indicated in Fig. 11, there exists in each case a so-called effective bond length ( $L_e$ ) over which the interfacial shear stresses are transferred to the steel substrate. The length of this active bond zone remains the same throughout the debonding process, though as mentioned earlier, it shifts toward the unloaded end of the strip.  $L_e$  was observed to be equal to approximately 115 mm in the Sika specimens, whereas a shorter  $L_e$  of 90 mm was obtained in both the 3M and EA-RT test specimens. The shortest value was observed in the EA-HR specimen, with  $L_e$  equal to approximately 70 mm. This further explains the slight differences among the obtained debonding loads, as the bonded interfaces that exhibited longer effective bond lengths demonstrated higher ultimate load levels. Furthermore, although identical epoxy adhesives were used in EA-RT and EA-HR, a shorter bond length was observed in the latter. This may be attributed to the effect of the high-temperature curing process on the behavior of such epoxy adhesives [25], which has been observed in CFRP-to-steel bonded joints [30] as well, and merits further investigation.

It is worth mentioning that a similar  $L_e$  range (i.e., 50–100 mm) was previously reported for NM CFRP plates (with comparable axial stiffness to that of the Fe-SMA used in this study), which were bonded to steel substrates using different epoxy adhesives [30,31]. However, one should pay careful attention to the fact that the effective bond length of an adhesively bonded reinforcement is highly dependent on its Young's modulus, as well as the adhesive and/or the substrate properties [29,32]. Therefore, a direct comparison between the expected  $L_e$  of Fe-SMA reinforcements with that of CFRP plates might not be necessarily correct, owing to the highly nonlinear behavior of the former. Further explanations and background information on the concept of effective bond length in adhesively bonded reinforcements can be found elsewhere [27,29,32].

The most obvious difference in the shear stress distributions of different specimens provided in Fig. 11 is the difference in the peak shear stresses. The peak shear stresses for Sika-1 are between 30 and 40 MPa, whereas those for EA-HR are above 60 MPa. As explained in Appendix A, some scattering in the calculated peak shear stresses is expected, which is also clearly shown in Fig. 11. It is highlighted that the peak shear stresses for all specimens shown in Fig. 11 are higher than the tensile lap shear strengths of the used adhesive (see

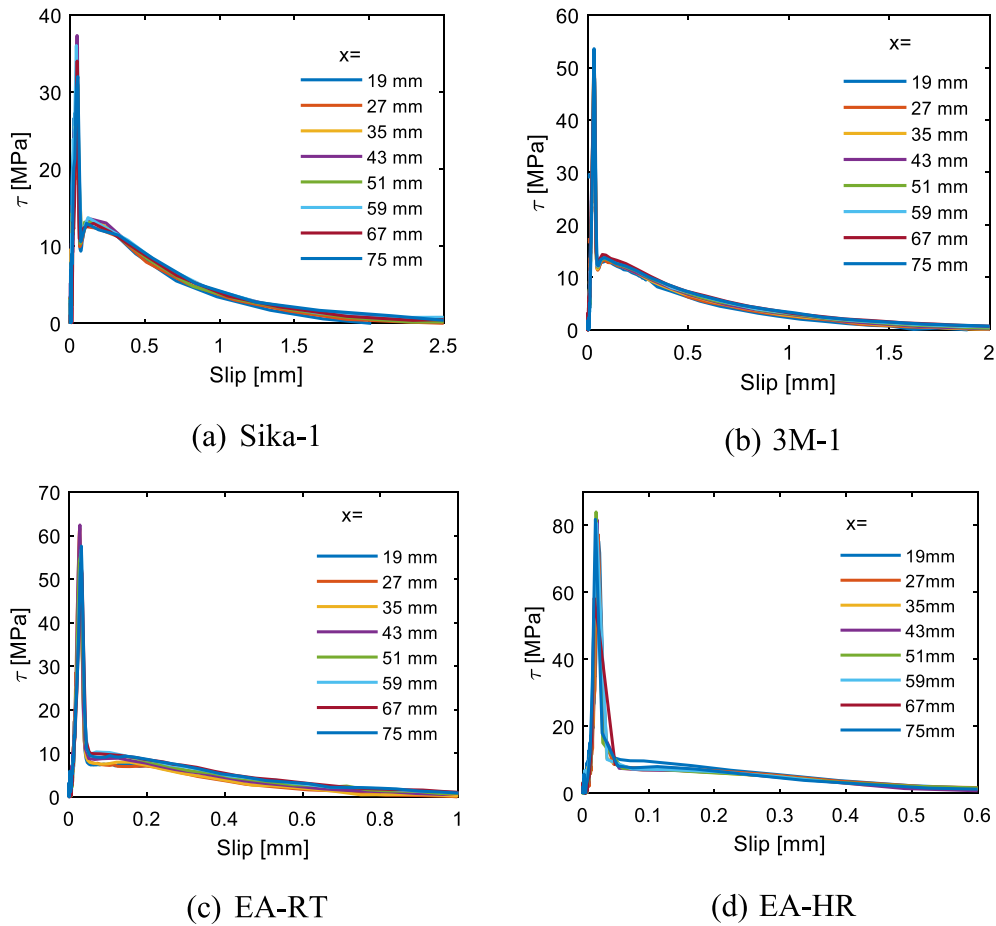


Fig. 13. Bond-slip behaviors.

Table 2) despite the scatters. This phenomenon is attributed to the stress relaxation mechanism in the Fe-SMA, which induces bias in the shear stresses calculated using Eq. (3). The creep strain induced by the stress relaxation in the Fe-SMA highly depends on the stress level and time [7]. For a crack tip between  $x_{i-1}$  and  $x_{i+1}$  as shown in Fig. 8, the creep strain at  $x_{i-1}$  is larger than that at  $x_{i+1}$  because the Fe-SMA at  $x_{i-1}$  has been subjected to a higher stress level for a longer time. This is manifested with specific data in Section 7.2. The creep strain contributes to the strain of the Fe-SMA and thus leads to an increase in the shear stress according to Eq. (3). However, one has to keep in mind that this increase in the shear stress does not have any physical meanings but is bias.

Another feature in the shear stress distributions that should be discussed is the observed kinks; a kink is more clearly shown in Fig. 12. As the shear stress is calculated based on the strains and stresses in the Fe-SMA strip using Eq. (3), a correlation between the strain and stress in the Fe-SMA strip, and the interfacial shear stress distribution is shown in Fig. 12 in order to explain the kink in the shear stress distribution. The different markers in this figure denote different locations along the x-axis. The Fe-SMA strip can be approximately split into a perfectly bonded area, the area over the FPZ, and a completely debonded area. The perfectly bonded area and the FPZ are divided by the splitting line at  $x = 94$  mm, as indicated by the dotted line in Fig. 12. The completely debonded area transfers no load from the Fe-SMA strip to the steel plate via shear stresses. The debonded area is deemed to span from the loaded end to approximately  $x = 50$  mm, where the shear stress level is almost zero (see Fig. 12). The shear stresses, strains, and axial stresses for locations where the peak shear stress and the kink lie are shown in Fig. 12.

As Fig. 12 shows, the strains are small for the Fe-SMA from the free end to  $x = 94$  mm and the shear stresses of the adhesive can still increase with increasing strains. This area is therefore regarded as the bonded area, i.e., the shear stress is at the ascending branch of the bond-slip relation (see Section 6). After the shear stress in the adhesive reaches the peak at  $x = 94$  mm, the shear strength is reached and it enters the softening region of the bond-slip relation, i.e., from 94 mm to approximately 50 mm, the shear stress in the bond line decreases as failure develops within the FPZ. At the same time, the strains and corresponding stresses in the Fe-SMA strip gradually approach the end of the linear part of the stress-strain curve of the Fe-SMA material. The adhesive cannot effectively restrain the deformation of the Fe-SMA owing to the reduced strength in the FPZ and the strain rapidly develops in the Fe-SMA from  $x = 94$  mm to the loaded end, i.e.,  $x = 0$  mm. As shown in Fig. 12, the strains and corresponding stresses at  $x = 92, 90, 88,$  and  $86$  mm are near the turning point in the stress-strain curve of the Fe-SMA material, where the Young's modulus decreases drastically. This highly nonlinear behavior of the Fe-SMA results in the kink in the shear stress distribution. In other words, the rapid development of strain in the Fe-

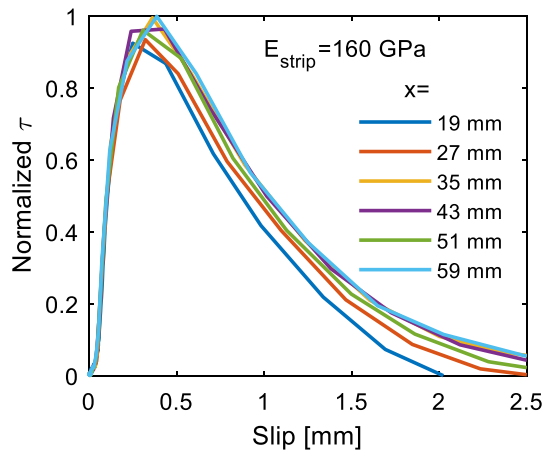


Fig. 14. Artificial bond-slip curves.

SMA does not lead to a rapid variation in the axial stresses. The shear stresses calculated using Eq. therefore do not continue to rapidly decrease, but rather vary slightly, thereby forming a kink in the distribution.

One should keep in mind that the stress relaxation mechanism of the Fe-SMA, as discussed in Section 4.5, contributes to the strain variation of the Fe-SMA strip over the FPZ. The coupled plastic deformation of the adhesive, plastic deformation of the Fe-SMA and pronounced stress relaxation over the FPZ lead to the shape of the kink where the shear stress decreases first and increases a bit. The variation of the shear stress at the kink is less than 5 MPa. The role of the stress relaxation mechanism in the calculated shear stress distribution and how the plastic deformations of the adhesive and the Fe-SMA are coupled must be further investigated by performing strain-controlled lap-shear tests and detailed finite element analysis.

6. Bond-slip behavior

The typical interfacial shear behaviors of the tested specimens, as characterized by the bond-slip relations, are summarized in Fig. 13. The bond-slip relations of specimens Sika-2 and 3M-2 are respectively very close to those of Sika-1 and 3M-1, as shown in Fig. 13(a) and (b). Finally, four bond-slip relations are presented and discussed in this section.

The bond-slip curve depicts the interfacial shear stress as a function of the relative displacement between the Fe-SMA strip and the steel plate (i.e., slip). For a given location,  $x_i$ , the slip and the shear stress are calculated with Eqs. (1) and (3). DIC images taken at different moments of the loading process for a series of crack lengths were post-processed to determine the relevant parameters in Eqs. (1) and (3).

It is noteworthy that only the joints with the Sika adhesive failed in the cohesive failure mode. The joints bonded with the Hysol EA9394 and 3M EC9323 adhesives failed in the adhesive failure mode at the interface between the Fe-SMA strip and the adhesive. The bond-slip relations are therefore not representative for the respective adhesives in these joints with the Hysol EA9394 and 3M EC9323 adhesives. Rather, they can be interpreted as the bond behavior between the adhesive and the Fe-SMA interface. Nevertheless, the

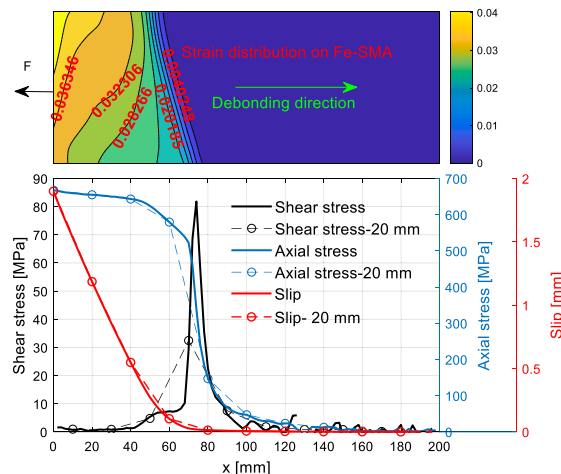


Fig. 15. Detailed experimental results of the specimen EA-HR.

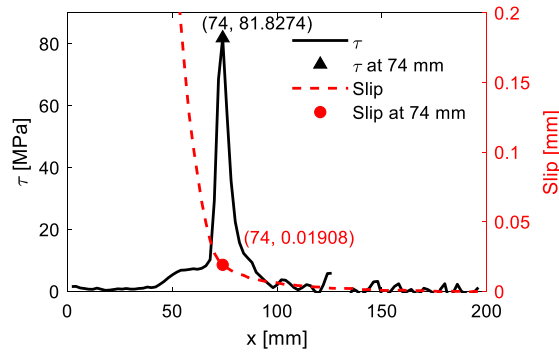


Fig. 16. Close-up of the shear stress and slip distributions (from Fig. 15).

Table 4

Data for obtaining the peak shear stress.

x [mm]	70	72	74	76	78
Axial stress [MPa]	522.71	460.49	339.83	242.29	185.14
Axial strain	0.0039	0.0027	0.0018	0.0013	0.0010
Slip [mm]	0.027	0.022	0.019	0.017	0.015
Shear stress [MPa]	29.24	68.58	81.83	58.01	35.73

bond–slip relations for all joints are shown and discussed in this section.

Fig. 13 shows that the bond–slip curves for all the specimens follow the same pattern. The shear stress increases linearly with the initially increasing slip until it reaches the peak shear bond stress,  $\tau_{max}$ , thereby forming a steep ascending branch of the bond–slip curve. The shear stress then drops sharply, and a kink appears in the bond–slip curve. Finally, the shear stress decreases gradually until it becomes zero at the final failure displacement,  $\delta_f$ . The formation of the kink in the bond–slip curve shares the same reason for the formation of kinks in the shear stress distribution curves explained in the previous section.

For the purpose of explanation, the strain and slip values used to obtain the bond–slip curves shown in Fig. 13(a) for specimen Sika-1 are reused to obtain artificial bond–slip curves for a strip with a constant Young’s modulus of 160 GPa (a reasonable value for NM CFRP plates). This artificially defined strip has the same thickness as the Fe-SMA strip tested. The bond–slip curves are shown in Fig. 14. The shear stress is normalized by 800 MPa. Evidently, the kink in Fig. 13(a) disappears in Fig. 14. This clearly explains that the drastic change in the Young’s modulus of the Fe-SMA results in the kink in the bond–slip curves. Of course, the shear stresses cannot develop as depicted in Fig. 14 in reality, because the development of the strains and slips would be different. Based on this observation, it can be reasonably argued that when a nonlinear Fe-SMA material is involved, the bond–slip curve is not characterized purely by the geometry of the joint and properties of the adhesive used.

Fig. 13 also shows that the bond–slip curves obtained at different locations overlap closely for the same specimen. It should be mentioned that the bond–slip relationship can be obtained at many different locations along the bond line in one single lap-shear test. The peak shear stress,  $\tau_{max}$ , and the failure displacement,  $\delta_f$ , vary for different joints with different adhesives. The EA-HR specimen has the highest  $\tau_{max}$  among all the specimens. Compared to the EA-RT specimen, the hot curing process for the EA-HR specimen improves the interfacial shear strength but reduces the slip at failure. Notably, the adhesive for these two specimens were not fully utilized, because the adhesive interface failure mode dominated. The bond–slip curves for the 3M-1 specimen are very similar to those for the Sika-1 specimen. Their bond strengths are also comparable. It is worth noting that the Sika-1 adhesive is very ductile with an ultimate tensile elongation of 4%, as listed in Table 2. For such a ductile adhesive, the bond-slip curve is expected to develop a trapezoidal shape [16], whereas the obtained bond-slip curves do not exhibit the shape. This is attributed to the coupled plastic deformations of the adhesive and the Fe-SMA adherend and the stress relaxation mechanism. Particularly the slip calculated by Eq. (1) comprises the deformation of the adhesive, the plastic deformation of the Fe-SMA and the deformation owing to the stress relaxation in the Fe-SMA. As shown in Fig. 10, the strain values of the steep gradient in the strain distribution indicate that the Fe-SMA was significantly plasticized. The significant plastic deformation contributes to the slip in the bond-slip relations.

It is emphasized that the experimentally obtained shear strengths have uncertainties, as explained in Appendix A. In addition, the stress relaxation of the Fe-SMA introduces errors in the calculated shear stresses, resulting in unexpectedly high shear stresses of all tested specimens.

## 7. Discussions

### 7.1. The limitations of the obtained bond-slip relations

The bond-slip relations have been obtained for all the tested specimens. From the perspective of fracture mechanics, the obtained

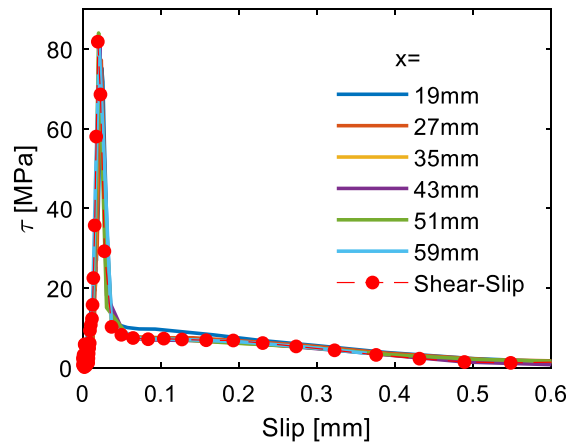


Fig. 17. Comparison of bond-slip relations.

bond-slip relations can be used for the fracture failure analysis of Fe-SMA bonded joints. The fracture energy,  $G_f$ , which is equal to the area enclosed by the bond-slip curve for the respective specimen, can be estimated. However, three energy dissipation mechanisms can be identified during the debonding process of the Fe-SMA bonded joints: debonding of the adhesive, plastic deformation of the Fe-SMA and stress relaxation of the Fe-SMA. Based on the energy balance principle, the fracture energy,  $G_f$ , should be equivalent to the total energy dissipation by the three mechanisms. As has been explained in the previous section, the shape of the obtained bond-slip relations are heavily affected by the coupled debonding of the adhesive, plastic deformation and stress relaxation of the Fe-SMA. It is therefore argued that the unexpected bond-slip relation is a result of the non-linear behavior of the Fe-SMA, as well as the debonding process of the adhesive.

Consequently, the bond strengths,  $P$ , of such joints cannot be predicted using the well-known equation, which is provided below [27]:

$$P = b_p \sqrt{2E_p t_p G_f} \quad (4)$$

where  $b_p$  is the width,  $E_p$  the modulus, and  $t_p$  the thickness of the strip. This equation was obtained mainly for CFRP-bonded joints, in which CFRP shows a linear elastic behavior up to failure [16,33]. Nevertheless, for the case of Fe-SMA bonded joints in this study, the modulus,  $E_p$ , drastically changes during the debonding process, leading to the inapplicability of Eq. (4). A more comprehensive fracture analysis frame is required in order to achieve an in-depth understanding of the failure behavior of the bonded Fe-SMA joints in which a debonding process is coupled with drastic non-linear behavior of the adherend. The contribution of each of the three mechanisms to the total energy dissipation needs to be carefully understood.

## 7.2. The relation between the bond-slip curve and the stress state at the crack tip

The shape of the bond-slip relation should reflect the stress state in the FPZ ahead of the (debonding) crack tip [34]. However, it has been a difficult task to characterize the stress state in the FPZ experimentally. The common practice is to assume a bilinear bond-slip relation with the approximately correct interfacial strength and fracture toughness to simulate the global load-displacement behavior [35]. Fortunately, the highly accurate DIC measurement results obtained in this research can be utilized to determine the relation between the bond-slip curves and the stress states in the tested specimen. In this section, a discussion based on the experimentally obtained results is provided.

In Fig. 15, the DIC measured strain distribution on the partially deboned Fe-SMA strip surface, post-processed distributions of axial stress, slip, and shear stress in the bond lines along the x-axis are presented. The results are for this specific crack length. The strain distribution is obtained directly from the DIC analysis. The post-processing techniques explained in Section 4.3 are used to obtain the slip, axial stress, and shear stress curves. To explain the effects of resolution further, in addition to the 4-mm data interval, which is the default interval used in this study (see Appendix A), an interval of 20-mm is also used. The solid lines are obtained with the 4-mm interval, and the dashed lines are obtained with the 20-mm interval. The 20-mm interval is chosen to represent the resolution of strain gauge measurements typically used in such tests [16].

Evidently, the strain values over the bonded area of the Fe-SMA are close to zero, whereas the values over the debonded area are fairly high. Notably, the strains increase near the loaded end, whereas an isostrain condition is expected in the completely debonded area. This can be explained by the relaxation mechanism of the Fe-SMA material, as discussed in Section 4.5. The loaded end area was debonded initially and the relaxation mechanism started to build up strains as the crack propagated. Consequently, a small strain gradient is observed on the completely debonded area of the Fe-SMA.

A steep gradient of the strain distribution is observed to be in close proximity to the crack tip, where the Fe-SMA transitions from a bonded state to a debonded state. The strain distribution is not exactly symmetric with respect to the horizontal middle line. The

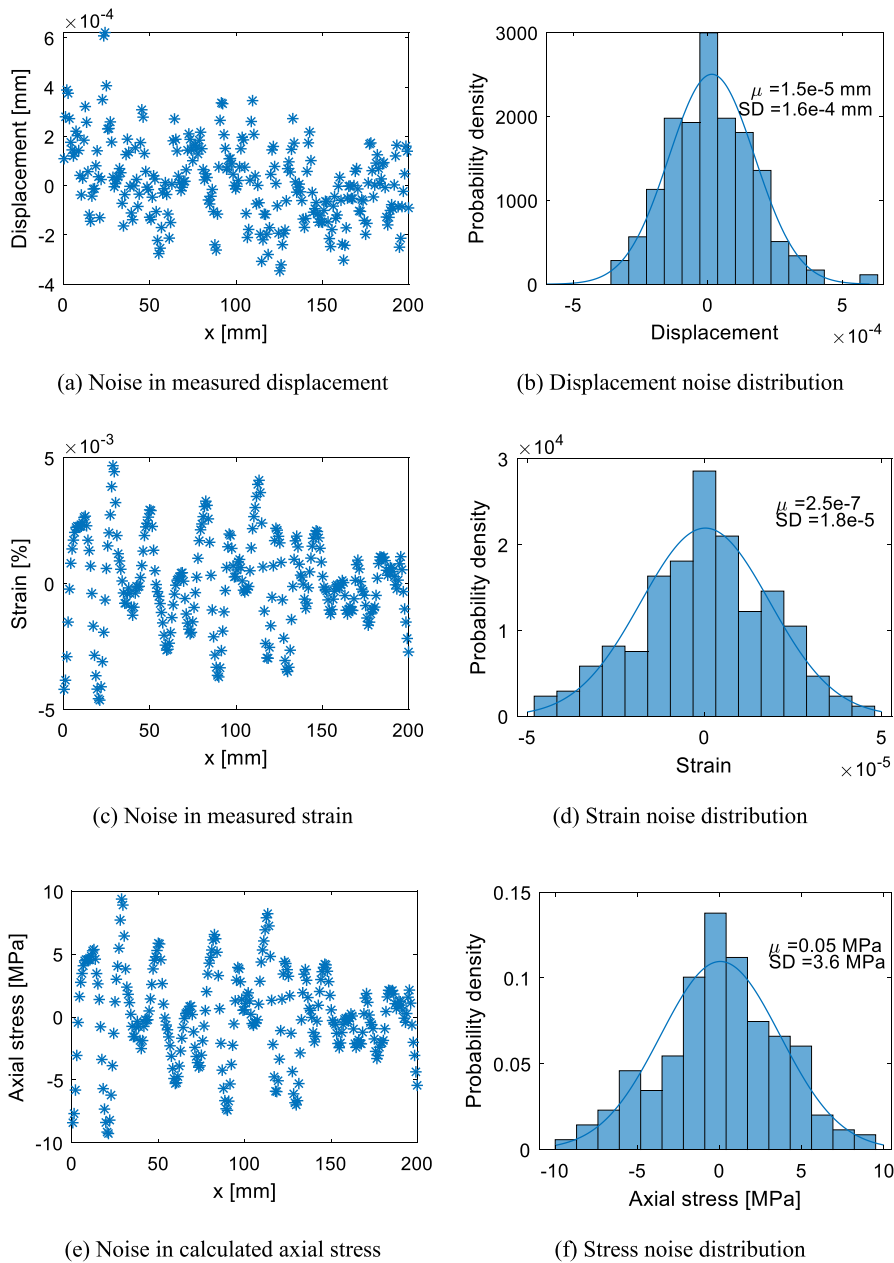


Fig. A1. Noises in the DIC measurements and calculated axial stresses ( $\mu$  indicates the mean value and  $SD$  indicates the standard deviation).

average of the strain values is used to obtain the curves in Fig. 15. This steep gradient in the strain distribution is reflected in the sharp drop in the solid axial stress curve and the peak in the solid shear stress curve. Additionally, the slope of the solid slip curve changes drastically in close proximity to the crack tip. The sharp drop in the axial stress occurs because the adhesive layer transfers the force in the Fe-SMA strip to the steel plate by shear within a short distance. Consequently, a high peak in the shear stress curve is observed. The successful capture of the steep gradients of the strain and axial stress distribution around the crack tip was made feasible with the high-resolution DIC equipment used in this research, whereas the dashed lines that represent the results obtained with virtual strain gauge measurements miss the detailed variation in the slip and axial stress distributions, particularly around the crack tip. The very coarse resolution fails to capture the details of the axial stress and slip distributions in the vicinity of the crack tip, as can be clearly observed from Fig. 15. The obtained shear stress distribution using this resolution is therefore quite different from that obtained with a high resolution. The peak shear stress obtained with the 20-mm interval is significantly lower. This is easily explained by the fact that the axial stresses at  $x = 60$  mm and  $80$  mm form a less steep slope than that of the solid axial stress curve and that the variation in the axial stress is averaged over a length of 20 mm to obtain the shear stress.

A close-up of the slip distribution and the shear stress distribution along x-axis in Fig. 15 is shown in Fig. 16. The shear stress

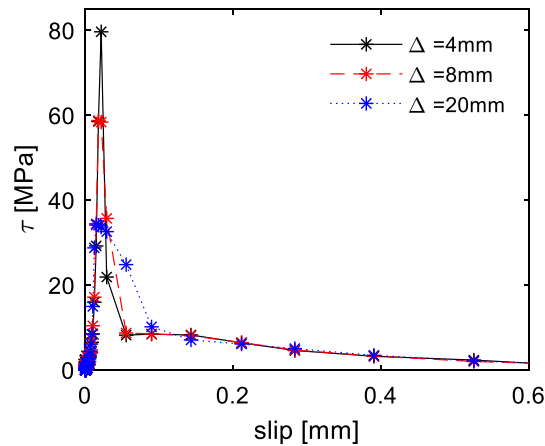


Fig. A2. Bond-slip relations as a function of interval.

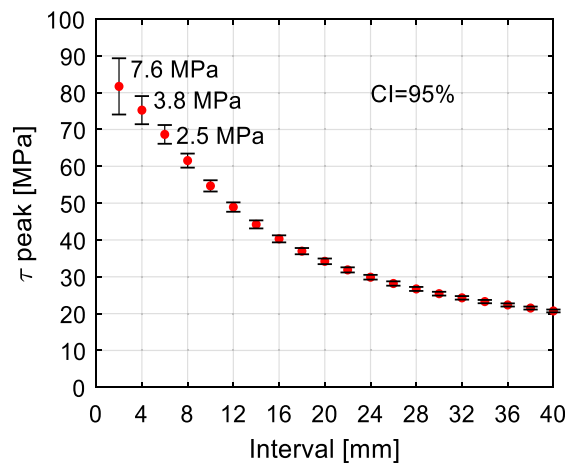


Fig. A3. Peak shear stress as a function of interval.

distribution appears to be an asymptotic line for the bonded portion of the joint as the shear stress increases from the free end to  $x = 74$  mm, where it reaches the maximum. Accordingly, the slip value also slowly increases. The slip starts to increase precipitously from  $x = 74$  mm to the loaded end as the adhesive cannot effectively restrain the slip, and the shear stress plunges owing to damage in the bond line.

The data shown in Fig. 15 is used to qualitatively analyze how much error can be introduced to the calculated peak shear stress for this adhesive. The data used to obtain the peak shear stress of 81.8 MPa at  $x = 74$  mm are listed in Table 4. The shear stress at  $x = 74$  mm is calculated based on the axial stresses at  $x = 72$  mm and  $x = 76$  mm according to Eq. (3). As can be seen from Table 4, the axial stress at  $x = 72$  mm is much higher than its counterpart. It has been demonstrated that the creep strain of the Fe-SMA at 400 MPa is slightly lower than 0.1% while that at 200 MPa stress level is close to 0 MPa after 1000 s holding time [7]. It is critical to understand that most of the creep strain develops in the first 100 s and its magnitude depends on the loading rate. The 0.1% creep strain can lead to above 30 MPa error in the shear stress calculated according to Eq. (3). This rough estimation merits further investigation on this topic.

The relationship between the shear stress distribution and the slip for this specific crack configuration should be reflected by the obtained bond-slip relation. Indeed, when the shear stress distribution in Fig. 15 is plotted against the slip distribution in Fig. 15 for the specific crack configuration, a bond-slip curve can be obtained and is compared to the bond-slip curves shown in Fig. 13(d) in Section 6. The comparison is presented in Fig. 17. As can be seen, the bond-slip relation obtained for the specific crack configuration matches the bond-slip curves perfectly. This proves that the shape of the bond-slip relation reflects the stress state in the FPZ ahead of the crack tip. A physical meaning can be assigned to the cohesive zone models.

### 8. Conclusions

For the first time, a systematic experimental study on the behavior of adhesively bonded Fe-SMA-to-steel joints was conducted and is presented herein. The DIC technique was used to monitor the debonding process, and the obtained test data were post-processed to

extract the bond–slip relations for the three adhesives tested.

The cohesive failure mode could be achieved with the Sika1277 adhesive and the bond strength is as high as 57 kN, which corresponds to approximately 76% of the ultimate strength of the tested Fe-SMA strip. All the adhesives tested can provide a bond capacity that is approximately twice the prestressing force achieved in the Fe-SMA upon activation and the tested joints exhibited an effective bond length ranging from 70 to 115 mm, showing that the adhesively bonded Fe-SMA joint is a promising solution for the fatigue strengthening of steel structures.

The techniques for obtaining the bond–slip relation for CFRP-to-steel joints have been employed to derive the bond–slip relation for the Fe-SMA-to-steel joints. It is found that the shapes of the bond–slip curves obtained in this study are influenced by the nonlinear behavior of the Fe-SMA. It is identified that the failure of the adhesive, the plastic deformation and stress relaxation of the Fe-SMA dissipate energy during the debonding process. The three energy dissipation mechanisms occurred simultaneously and were coupled to shape the bond–slip curves.

It is still questionable to use the obtained bond–slip curves for predicting the failure of bonded Fe-SMA joints. More advanced research is required to understand the failure process and how the plastic deformation and stress relaxation of the Fe-SMA contribute to the energy dissipation. The well-established fracture analysis for analyzing the debonding of FRP-to-steel joints are inadequate for an in-depth and accurate analysis of the debonding behavior of the Fe-SMA-to-steel joints. An advanced fracture analysis frame is therefore required to take the three energy dissipation mechanisms into consideration.

### Declaration of Competing Interest

The authors declare that they have no known competing financial interests or personal relationships that could have appeared to influence the work reported in this paper.

### Acknowledgements

The authors are grateful for the financial support from Innosuisse Swiss Innovation Agency and re-fer AG Company under the project number 30060.1 IP-ENG. It should be noted that all the commercial product names mentioned in this paper are only provided for the sake of factual accuracy, and references thereto should not necessarily be interpreted as endorsements of the products.

### Data availability

The raw/processed data required to reproduce these findings cannot be shared at this time as the data also forms part of an ongoing study.

### Appendix A

It is a common practice to calculate the shear stress in the bond line with Eq. for single lap-shear tests. A crucial task is to specify the interval,  $\Delta = x_{i+1} - x_{i-1}$ , between two axial stress data points,  $\sigma_{i+1}$  and  $\sigma_{i-1}$ , which are used to calculate the shear stress. It is generally acknowledged that the interval should not be too large, to ensure that a reasonably high shear strength and a high shear stress gradient are captured. On the one hand, if  $\Delta$  were larger than the effective bond length, then the shear strength would be significantly underestimated. On the other hand, it had not been quantitatively specified in the open literature how small the intervals should be. This ambiguity is largely due to the low accuracy and precision of DIC measurements or the limitation in the spatial resolution of strain gauges employed in previously reported lap-shear tests.

This section presents a discussion on how the interval is specified for the data post-processing in this study. Two factors are considered in specifying the interval: (1) the noise levels in the DIC measurements and calculated shear stresses, and (2) the spatial resolution, which should be sufficiently high to capture the high shear stress gradient in the FPZ zone. This is only achievable thanks to the highly accurate DIC system with a precisely controlled calibration and measuring process used in this research.

First, the accuracy and precision of the DIC measurements are estimated. Several images of unloaded specimens in addition to the reference image were acquired for the analysis of noise levels in the DIC measurements. The images were analyzed using the Vic-3D 8 software to obtain the displacements and strains on the Fe-SMA strip surface. It was found that the spatial resolution of the DIC measurement is as small as 0.75 mm for the setup used in this study. Consequently, more than 260 data points, averaged at each section, corresponded to over 200-mm used for this measurement error analysis. Because the specimen was not loaded, the true values of the displacement and strains should be zero. The displacement and strain values obtained from the DIC are therefore noises in the measurements; typical results are shown in Fig. A.1(a) and (c). As can be observed, the displacements and strain values oscillate around zero. The corresponding distributions of the displacement and strain noises are depicted in Fig. A.1(b) and (d), respectively. It can be further observed that they follow the normal distribution perfectly, which further confirms that they are measurement noises. Additionally, the mean displacement and strain values are nearly zero with small standard deviation (SD) values.

The measurement errors in the strains lead to errors in the calculated axial stresses in the Fe-SMA. The axial stresses in the unloaded Fe-SMA strip are calculated based on the DIC strain measurements. For a conservative uncertainty calculation in this section, the initial Young's modulus of the Fe-SMA of 200 GPa was used to calculate the stresses. The measured axial stresses along the free-stress Fe-SMA strip are presented in Fig. A.1(e) and the distribution is shown in Fig. A.1(f). The SD of the stress noises is 3.6 MPa.

The errors in the axial stresses of the Fe-SMA propagate into the calculated shear stresses through Eq. (3). For simplicity and

conservatism, the axial stress values at two locations,  $\sigma_{i+1}$  and  $\sigma_{i-1}$ , are assumed to be independent variables with errors following the same normal distribution. The standard deviation of the errors in the calculated shear stress can be calculated as follows:

$$SD_{\tau} = \sqrt{2 \left( \frac{t_{Fe-SMA}}{\Delta} \right)^2 SD_{\sigma}^2} = \sqrt{2} \frac{t_{Fe-SMA}}{\Delta} SD_{\sigma} \quad (5)$$

where  $SD_{\tau}$  and  $SD_{\sigma}$  are standard deviations in the shear stresses and tensile axial stresses, respectively.

Second, the effect of the interval length on the bond–slip relation is examined. The bond–slip relations of the test at locations  $x = 100$  are presented for three different interval lengths in Fig. A.2. It is evident that the interval length has a huge influence on the experimentally determined peak shear stress. An interval of 4 mm provides a peak shear stress twice as high as that of a 20-mm interval. This can be interpreted in terms of spatial resolution. A smaller interval length means a higher spatial resolution of the measurement, allowing for capturing the steep axial stress gradient on the Fe-SMA strip in close proximity to the debonding crack tip. A high peak shear stress calculated using Eq. (3) results from the successful capture of the steep axial stress gradient. Another important observation is that the initial slope of the bond–slip relations is the same for intervals spanning from 4 to 20 mm.

In Fig. A.3, the mean values of calculated peak shear stresses using different intervals for 40 different locations along the x-axis of the Fe-SMA are plotted against the interval. A prominent trend can be observed: the shear strength increases as the interval decreases. This confirms that a smaller interval captures the steep axial stress gradient better, and therefore, a higher shear stress peak is obtained.

It is noteworthy that the calculated shear stress peak also contains uncertainty. The errors in the axial stresses can propagate into the calculated shear stresses, which is determined by Eq. (5). It can be easily understood that the SD of the calculated shear strengths is inversely proportional to the interval  $\Delta$ . When  $\Delta < \sqrt{2}t_{Fe-SMA}$ , the uncertainty in the estimated shear strength is amplified. Error bars with a 95% confidence interval are added to the estimated shear strengths in Fig. A.3. The errors are twice the SD calculated by Eq. (5). Clearly, the errors increase as the intervals decrease.

A trade-off is made between the spatial resolution and the noise levels in this study. The interval of 4 mm is chosen for all the data analysis in this study.

## References

- [1] Zheng B, Dawood M. Fatigue strengthening of metallic structures with a thermally activated shape memory alloy fiber-reinforced polymer patch. *J Compos Constr* 2017;21(4):04016113.
- [2] El-Tahan M, Dawood M, Song G. Development of a self-stressing NiTiNb shape memory alloy (SMA)/fiber reinforced polymer (FRP) patch. *Smart Mater Struct* 2015;24(6):065035.
- [3] Hosseini A, Ghafoori E, Motavalli M, Nussbaumer A, Zhao X-L. Mode I fatigue crack arrest in tensile steel members using prestressed CFRP plates. *Compos Struct* 2017;178:119–34.
- [4] Dong Z, Klotz UE, Leinenbach C, Bergamini A, Czaderski C, Motavalli M. A novel Fe-Mn-Si shape memory alloy with improved shape recovery properties by VC precipitation. *Adv Engng Mater* 2009;11(1–2):40–4.
- [5] Mohd Jani J, Leary M, Subic A, Gibson MA. A review of shape memory alloy research, applications and opportunities. *Mater Des (1980–2015)* 2014;56:1078–113.
- [6] Hosseini A, Michels J, Izadi M, Ghafoori E. A comparative study between Fe-SMA and CFRP reinforcements for prestressed strengthening of metallic structures. *Constr Build Mater* 2019;226:976–92.
- [7] Leinenbach C, Lee WJ, Lis A, Arabi-Hashemi A, Cayron C, Weber B. Creep and stress relaxation of a FeMnSi-based shape memory alloy at low temperatures. *Mater Sci Engng, A* 2016;677:106–15.
- [8] Lee WJ, Weber B, Feltrin G, Czaderski C, Motavalli M, Leinenbach C. Stress recovery behaviour of an Fe–Mn–Si–Cr–Ni–VC shape memory alloy used for prestressing. *Smart Mater Struct* 2013;22(12):125037.
- [9] Ghafoori E, Hosseini E, Leinenbach C, Michels J, Motavalli M. Fatigue behavior of a Fe-Mn-Si shape memory alloy used for prestressed strengthening. *Mater Des* 2017;133:349–62.
- [10] Izadi MR, Ghafoori E, Shahverdi M, Motavalli M, Maalek S. Development of an iron-based shape memory alloy (Fe-SMA) strengthening system for steel plates. *Engng Struct* 2018;174:433–46.
- [11] Izadi MR, Ghafoori E, Motavalli M, Maalek S. Iron-based shape memory alloy for the fatigue strengthening of cracked steel plates: effects of re-activations and loading frequencies. *Engng Struct* 2018;176:953–67.
- [12] Izadi M, Motavalli M, Ghafoori E. Iron-based shape memory alloy (Fe-SMA) for fatigue strengthening of cracked steel bridge connections. *Constr Build Mater* 2019;227:116800.
- [13] Izadi M, Hosseini A, Michels J, Motavalli M, Ghafoori E. Thermally activated iron-based shape memory alloy for strengthening metallic girders. *Thin-Walled Struct* 2019;141:389–401.
- [14] Fritsch E, Izadi M, Ghafoori E. Development of nail-anchor strengthening system with iron-based shape memory alloy (Fe-SMA) strips. *Constr Build Mater* 2019;229:117042.
- [15] Wang W, Lopes Fernandes R, Teixeira De Freitas S, Zarouchas D, Benedictus R. How pure mode I can be obtained in bi-material bonded DCB joints: a longitudinal strain-based criterion. *Compos B Engng* 2018;153:137–48.
- [16] Yu T, Fernando D, Teng JG, Zhao XL. Experimental study on CFRP-to-steel bonded interfaces. *Compos B Engng* 2012;43(5):2279–89.
- [17] Shahverdi M, Michels J, Czaderski C, Motavalli M. Iron-based shape memory alloy strips for strengthening RC members: material behavior and characterization. *Constr Build Mater* 2018;173:586–99.
- [18] Hosseini E, Ghafoori E, Leinenbach C, Motavalli M, Holdsworth SR. Stress recovery and cyclic behaviour of an Fe–Mn–Si shape memory alloy after multiple thermal activation. *Smart Mater Struct* 2018;27(2):025009.
- [19] El-Tahan M, Dawood M. Bond behavior of NiTiNb SMA wires embedded in CFRP composites. *Polym Compos* 2018;39(10):3780–91.
- [20] Wang H-T, Wu G, Pang Y-Y, Shi J-W, Zakari HM. Experimental study on the bond behavior between CFRP plates and steel substrates under fatigue loading. *Compos B Engng* 2019;176:107266.
- [21] Wang H-T, Wu G, Dai Y-T, He X-Y. Experimental study on bond behavior between CFRP plates and steel substrates using digital image correlation. *J Compos Constr* 2016;20(6):04016054.
- [22] Wang W, Poulis JA, Freitas STD, Zarouchas D. Surface pretreatments on CFRP and titanium for manufacturing adhesively bonded bi-material joints. In: *ECCM18 - 18th European Conference on Composite Materials*. 2018: Athens, Greece.

- [23] Hysol EA 9394 Technical data sheet. 2850 Willow Pass Road, CA, USA: Henkel Corporation Aerospace.
- [24] SikaPower-1277 Product data sheet. Zurich, Switzerland: Sika Services AG; 2018.
- [25] Hosseini A, Michels J. Glass transition evaluation of commercially available epoxy adhesives for strengthening of steel structures with bonded CFRP plates. In: 9th international conference on fibre-reinforced polymer (FRP) composites in civil engineering (CICE 2018). Paris, France; 2018.
- [26] 3M™ Scotch-Weld™ EC-9323 B/A Technical data sheet. 3M Automotive and Aerospace Solutions Division European Aerospace Laboratory.
- [27] Fernando ND. Bond behaviour and debonding failures in CFRP-strengthened steel members. Kowloon, Hongkong: The Hong Kong Polytechnic University; 2010.
- [28] Wang W, Rans C, Alderliesten RC, Benedictus R. Predicting the influence of discretely notched layers on fatigue crack growth in fibre metal laminates. *Engng Fract Mech* 2015;145:1–14.
- [29] Martinelli E, Hosseini A, Ghafoori E, Motavalli M. Behavior of prestressed CFRP plates bonded to steel substrate: numerical modeling and experimental validation. *Compos Struct* 2019;207:974–84.
- [30] Hosseini A, Ghafoori E, Wellauer M, Sadeghi Marzaleh A, Motavalli M. Short-term bond behavior and debonding capacity of prestressed CFRP composites to steel substrate. *Engng Struct* 2018;176:935–47.
- [31] Hosseini A, Ghafoori E, Al-Mahaidi R, Zhao X-L, Motavalli M. Strengthening of a 19th-century roadway metallic bridge using nonprestressed bonded and prestressed unbonded CFRP plates. *Constr Build Mater* 2019;209:240–59.
- [32] Hosseini A, Mostofinejad D. Effective bond length of FRP-to-concrete adhesively-bonded joints: experimental evaluation of existing models. *Int J Adhes Adhes* 2014;48:150–8.
- [33] Teng JG, Yu T, Fernando D. Strengthening of steel structures with fiber-reinforced polymer composites. *J Constr Steel Res* 2012;78:131–43.
- [34] Shet C, Chandra N. Effect of the shape of T- $\delta$  cohesive zone curves on the fracture response. *Mech Adv Mater Struct* 2004;11(3):249–75.
- [35] Harper PW, Hallett SR. Cohesive zone length in numerical simulations of composite delamination. *Engng Fract Mech* 2008;75(16):4774–92.